RESEARCH PAPER

Evolution of mixing in a microfluidic reverse-staggered herringbone micromixer

Brian Hama[1] · Gautam Mahajan[1] · Petru S. Fodor[2] · Miron Kaufman[2] · Chandrasekhar R. Kothapalli[1]

Abstract

Microfluidic platforms offer a variety of advantages including improved heat transfer, low working volumes, ease of scale-up, and stronger user control on operating parameters. However, flow within microfluidic channels occurs at low Reynolds number (*Re*), which makes mixing difficult to accomplish. Adding V-shaped ridges to channel walls, a pattern called the staggered herringbone design (SHB), alleviates this problem by introducing transverse flow patterns that enable enhanced mixing. Building on our prior work, we here developed a microfluidic mixer utilizing the SHB geometry and characterized using CFD simulations and complimentary experiments. Specifically, we investigated the performance of this type of mixer for unequal species diffusivities and inlet flows. A channel design with SHB ridges was simulated in COMSOL Multiphysics® software under a variety of operating conditions to evaluate its mixing capabilities. The device was fabricated using soft-lithography techniques to experimentally visualize the mixing process. Mixing within the device was enabled by injecting fluorescent dyes through the device and imaging using a confocal microscope. The device was found to efficiently mix fluids rapidly, based on both simulations and experiments. Varying *Re* or species diffusion coefficients had a weak effect on the mixing profile, due to the laminar flow regime and insufficient residence time, respectively. Mixing effectiveness increased as the species flow rate ratio increased. Fluid flow patterns visualized in confocal microscope images for selective cases were strikingly similar to CFD results, suggesting that the simulations serve as good predictors of device performance. This SHB mixer design would be a good candidate for further implementation as a microfluidic reactor.

Keywords Microfluidic mixer · Staggered Herringbone design · COMSOL · Mixing index · Confocal microscopy

1 Introduction

Microfluidics, the study of the behavior and manipulation of fluids in channels consisting of inner dimensions of less than 1 mm (Ehrfeld et al. 2000), has gained interest over the past 2 decades, because it enables the miniaturization of processes and systems (Giuffrida and Spoto 2017) with applications in clinical diagnostics (Bellassai and Spoto 2016), food security (Spoto and Corradini 2012), biological processing (Sudarsan and Ugaz 2006), chemical reaction control (Günther and Jensen 2006), among others (Jeong et al. 2009). The small dimensions increase the surface area-to-volume ratio within microfluidic channels by two to three orders of magnitude (Ehrfeld et al. 2000), which significantly increases control over variables in chemical reactions such as temperature, pressure, volume, and mass transport (Makgwane and Ray 2014). Conditions in these small volumes are also more uniform, which suppresses temperature and concentration gradients. Reactions also become inherently safer (Janasek et al. 2006), because overall volumes are much lower, and runaway exothermic reactions can be better controlled due to enhanced heat transfer. Furthermore, scale-up for production at industrial levels becomes considerably easier. The rigorous process of scaling a laboratory reactor to full size could be circumvented by numbering up, i.e., using a large number of smaller devices to increase production (Hessel et al. 2008).

✉ Chandrasekhar R. Kothapalli
c.kothapalli@csuohio.edu

[1] Department of Chemical and Biomedical Engineering, Cleveland State University, Cleveland, OH 44115, USA

[2] Department of Physics, Cleveland State University, Cleveland, OH 44115, USA

Of the many unit operations that can be realized in microfluidic devices, mixing is of particular interest, because it is a necessity to perform chemical reactions or develop formulations. However, mixing in microfluidics is difficult, because the flow is highly laminar ($Re \leq 100$), which hinders material from being effectively transported across fluid layers (Kamholz et al. 2001). Consequently, diffusion is the only mechanism of mass transport which takes place on much longer time scales than convection (Tan et al. 2005).

Methods of inducing mixing in microfluidic devices could be classified as active or passive. In active mixers, some external source (Yaralioglu et al. 2004) of fluid agitation is employed; examples include electrophoresis (Nguyen and Wu 2005; Salmanzadeh et al. 2011), magneto-hydrodynamic particles (Nguyen and Wu 2005), addition of artificial cilia (Toonder et al. 2008), pressure fields (Glasgow and Aubry 2003), acoustics (Yang et al. 2001), and temperature manipulation (Tsai and Lin 2001). Although active micromixers are usually considered more efficient than passive mixers (Wu and Nguyen 2005), they tend to be difficult to implement in practice due to the need for external equipment and power sources (Capretto et al. 2011). Passive mixers, favored in numerous applications, utilize special channel designs that disrupt the orderly laminar flow to increase contact area between the two fluids and reduce the diffusion length (Capretto et al. 2011). Typically, passive mixers utilize T-shaped mixing channels, hydrodynamic focusing, chaotic advection (F-shaped channel arrangements, two-layer crossing channel mixers, and 3D serpentine designs), slanted groove mixer (SGM), and staggered herringbone (SHB) type designs (Erbacher et al. 1999; Fodor et al. 2009; Fodor and Kaufman 2011; Itomlenskis et al. 2008; Johnson et al. 2002; Kamholz et al. 1999; Knight et al. 1998; Lee et al. 2006; Li et al. 2012; Nimafar et al. 2012; Özbey et al. 2016; Stremler et al. 2004; Stroock et al. 2002; Xia et al. 2005).

In the geometry investigated as part of this study, i.e., the SHB, a set of grooves with the shorter end on the left-hand side is followed by another set of grooves with the short end on the right-hand side to complete one mixing cycle, which could be repeated many times throughout a device. The forward SHB arrangement features the ridges with their vertices pointing against the flow and is commonly reported in the literature; the opposite orientation (i.e., vertices pointing in the direction of flow) is referred to as the reverse SHB mixer (Williams et al. 2008). In both CFD simulations (Kee and Gavriilidis 2008; Williams et al. 2008) and experiments (Du et al. 2010), the forward SHB geometry has been shown to be effective at mixing fluids by adding rotational and extensional flows (Stroock et al. 2002). In general, the specifics of the design and operation of SHB microfluidic mixers vary depending on the desired application (Williams et al. 2008).

A comprehensive comparison between the forward and reverse configurations, as well as those with ridges raised into the channels versus recessed into the walls, has been reported (Kwak et al. 2016). The normalized intensity profile within channels was reported from fluorescence microscopy images, although quantification of mixing was lacking. When the forward and reverse SHB designs with positive or negative reliefs were compared (Kwak et al. 2016), it was concluded that there is no significant difference in mixing efficiency between the forward and reverse configurations with positive relief pattern of the design, and that the required number of cycles for complete mixing in positive-forward or positive-reverse was the same (3 cycles); however, the reverse pattern had a higher directional transfer effect than the forward pattern. Nevertheless, the role of fluid characteristics on the evolution of mixing efficiency in reverse SHB remained unexplored, which formed the basis for this study.

The design of the ridges in a SHB mixer, i.e., the shape, inter-ridge spacing, and overall dimensions, varies greatly across different studies. The influence of mixer design parameters, such as ridge and channel depth/width, inter-ridge spacing, location of the ridge vertex, and relative height of channel compared to the ridges, was previously reported (Du et al. 2010; Itomlenskis et al. 2008; Stroock et al. 2002). Although CFD simulations largely treat Re as the primary variable for mixing evaluations, other mixing fluids characteristics such as diffusivities of species or the inlet species flow rates affect mixing performance of SHB mixer, which remains unexplored.

The objective of this study is to address this gap in the literature towards implementation of a reverse-staggered herringbone mixer for applications which demand thorough mixing within the channel. The mixer geometry was designed in SolidWorks® and simulated with COMSOL Multiphysics® software. Simulation results were compared to and validated in selective cases by confocal microscopy images obtained under similar conditions in situ within the fabricated device.

2 Theory—mixer design

The micromixer was first designed in SolidWorks® as two separate layers, to be combined in fabrication. The top layer contained the main channel, rectangular in shape with a width of 200 μm and height of 50 μm (Figs. 1, 2). The bottom layer of the main channel comprised of 50-μm-deep SHB ridges. The ridges were asymmetrical and spanned the width of the channel, and one complete mixing cycle was 1886 μm in length. The main channel contained nine complete cycles. The cartesian coordinate system was defined for a single straight channel with the origin at the bottom left
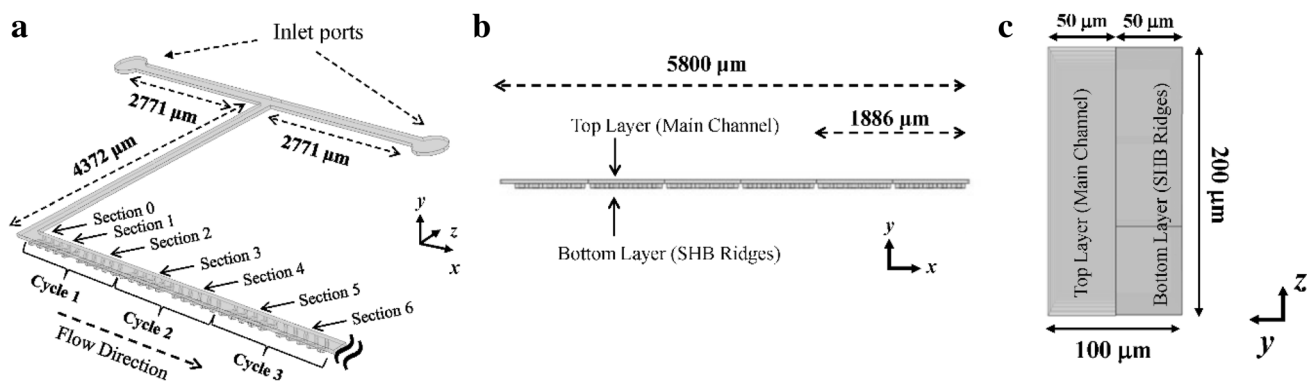
Fig. 1 Schematic of the SHB micromixer design developed for this study. Three complete mixing cycles taken from different orientations in COMSOL. The direction of flow is along the *x*-direction and the height is in *y*-direction. **a** Angled view indicating the defined cycles and sections along the channel length. Also shown were side view from *x–y* plane (**b**) and cross-sectional view from *y-z* plane (**c**)
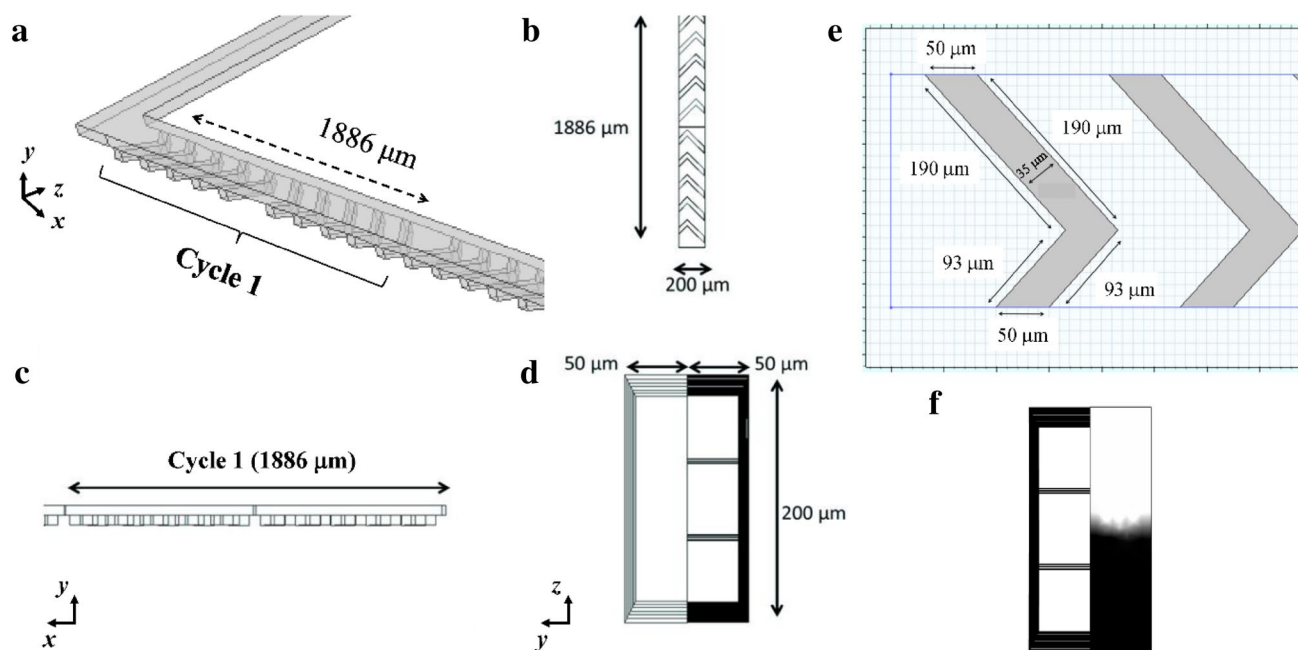
Fig. 2 **a** Close diagonal view of the first mixing cycle. The channels were also shown in the *x–z* plane (**b**), *x–y* plane (**c**), and *y–z* plane (**d**), with dimensions indicated. **e** Enlarged view of a typical herringbone ridge, with dimensions indicated. **f** Inlet concentration profile created by the described step change across the channel. The resulting profile was the same when two separate inlets of pure fluid are merged at this location

corner of the main channel inlet (Fig. 1a). The device was oriented, so that all channels were at the same elevation, and therefore, hydrostatic effects were neglected. Finally, there is no accumulation or depletion of material in the device.

The device performance was evaluated using COMSOL Multiphysics® 5.2 simulation software with a Chemical Engineering Module. The studies conducted on the device utilized the Laminar Flow (SPF) and Transport of Diluted Species (TDS) physics interfaces. The TDS interface was configured to handle the two species to be mixed. The device

was assumed to be operating at steady state, and one set of time-dependent studies was performed to observe the transient conditions prior to steady state. The fluid was assumed incompressible and Newtonian, and the physical properties approximated to water (i.e., $\rho = 1000$ kg/m^3 and $\mu = 0.001$ Pa•s). Two dilute species, A and B, are to be mixed in the main channel, and they would enter the device from designated inlet ports at varying concentrations, diffusivities (depending on M_w), and flow rates. The species diffusivity is assumed to be that of FITC–Dextran

(e.g., 10 μM) at 25 °C. Four molecular weights (1, 10, 100, and 1000 kDa) with corresponding diffusivities ($D_i = 29.1 \times 10^{-11}$ m²/s, 9.25×10^{-11} m²/s, 3.16×10^{-11} m²/s, and 1.1×10^{-11} m²/s, respectively) (Kothapalli and Honarmandi 2014) were considered, with each diffusion coefficient designated by its molecular weight (i.e., $D1$, $D10$, $D100$, and $D1000$).

The channel geometry for the first mixing cycle is shown in Fig. 2. The ridges are 35-μm-wide and recessed into the lower wall 50-μm-deep (Fig. 2e). One section is defined as a grouping of five consecutive identical ridges, with one complete mixing cycle consisting of two sections: one with the vertices left of center and one with the vertices right of center. The boundary and operating conditions are summarized in Table 1 and Fig. SI-1. Inlet flow was for $Re = 0.01$, 0.1, 1, 10, and 100 (all in laminar range). The corresponding flow rates were divided between species A and B. R_{AB}, defined as the ratio of flow rate of species A to that of species B, was varied from 1 to 3. The inlet concentration profile is a step change along the z-direction defined with respect to an initial concentration $c_{0A} = c_{0B} = 10$ μM: $c_A = c_{0A}$ for $0 < z \leq 100$ μm, $c_A = 0$ for $100 < z \leq 200$ μm, $c_B = 0$ for $0 < z \leq 100$ μm, $c_B = c_{0B}$ for $100 < z \leq 200$ μm. The no-slip condition applies to all walls in the device, while the flow is pressure-driven and exits to atmospheric pressure (outlet gauge pressure is zero).

In this study, the channels were rectangular, so the characteristic length is evaluated according to definition, $L = 4(A_c/P_w)$, where A_c and P_w are the cross-sectional area and wetted perimeter of the channel, respectively (Welty et al. 2008). For a rectangular duct with width a and height b, the characteristic length can be computed as $L = 2\left(\frac{ab}{a+b}\right)$.

To solve the fluid velocity profile in this channel geometry, the Navier–Stokes equation of motion and continuity equation for momentum transport were employed for an incompressible fluid with no accumulation (McCabe et al. 2004) (Fig. SI-1). Similarly, in this device, mass transport occurs due to both diffusion and convection, and so the convection–diffusion equation was used as the governing model for mass transport (Bird et al. 2006). The Péclet number quantifies the relative importance of convective and diffusive terms (McCabe et al. 2004), defined as $Pe = uL/D_i$, and $Pe > 1$ suggests that convection is more significant than diffusion.

3 Materials and methods

3.1 CFD simulations

Simulations were performed for the first three mixing cycles in this study, and the two separate inlet channels that lead up to the first mixing cycle were omitted except for the cases where Re and R_{AB} were varied. The inlet was constructed as a single stream of fluid incorporating the previously described stepwise change in concentration. Preliminary testing showed that both geometrical configurations (with and without inlet channels) led to similar results (< 1% deviation). Simulations involving a geometry twice this length (six mixing cycles) were also performed to test whether more mixing cycles (beyond 3 cycles) would result in a higher mixing efficiency. The geometry was divided into a mesh of tetrahedral elements containing 524,000 domains, 64,000 boundaries, and 6000 edges. Although finer meshes yielded higher resolution in the simulation results, it increased the computational demand. These mesh characteristics were optimized by trial and error.

Initially, a two-step stationary study (or steady state) was created: the first step utilized the SPF physics interface and its settings, while the second step used SPF results in combination with the TDS interface to compute the concentration profile. All computations in this work employed the Generalized Minimum Residual (GMRES) method of solving the system. The device geometry was also simulated under non-steady-state conditions to gain an understanding of how mixing was established upon initiating the flow. A similar simulation was used for creating a time-dependent study, by selecting a range of time points, to observe the development of the steady-state concentration profile and determine approximately how much time was required to achieve this. Table 2 lists the various conditions examined using CFD simulations including variables manipulated and held constant. For the four diffusion coefficient values considered in Study 3, there were ten non-repeating pairs of D_i between the two species A and B (listed in Supplementary Table 1).

3.2 Mixing quality evaluation

Cross-sectional images of the concentration profile were captured at various y–z planes of the mixing cycles, which were used to evaluate the mixing index, M. A statistical approach was used to determine M by evaluating the Shannon Entropy (Camesasca et al. 2005). This method

Table 1 Summary of the boundary conditions used for solving the fluid flow in COMSOL

Boundary condition type	Details
Inlet flow	$Re = 0.01$, 0.1, 1, 10, 100 $u = 0.125$, 1.25, 12.5 cm/s
Species flow rate ratio	$R_{AB} = 1, 2, 3$
Inlet concentration	$c_{0A} = c_{0B} = 10$ μM
Wall effects	No-slip; $u = 0$ at walls
Pressure	$P_{outlet} = 0$

Table 2 List of studies performed in COMSOL with manipulated and constant quantities

Study	Description	Variables manipulated	Variables held constant
1	Re Sweep	$Re = 0.01, 0.1, 1, 10, 100$	$D_A = D_B = D1; R_{AB} = 1$
2	Extended channel	Number of mixing cycles	$Re = 1; D_A = D_B = D1; R_{AB} = 1$
3	Diffusivity sweep	$D_i = D1, D10, D100, D1000$	$Re = 1; R_{AB} = 1$
4	R_{AB} Sweep	$R_{AB} = 1, 2, 3; Re = 0.1, 1, 10, 100$	$D_A = D_B = D10$
5	Transient study	$Re = 0.1, 1, 10, 100$	$D_A = D_B = D1; R_{AB} = 1$

depends on the probability distribution of intensities from a grayscale fluorescence image (Kaufman et al. 2007):

$$S_j(\text{species}) = -\sum_{c=1}^{2} p_{c/j}\ln(p_{c/j}) \tag{1}$$

$$S_{\text{locations}}(\text{species}) = \sum_{j=1}^{N} p_j S_j(\text{species}), \tag{2}$$

where S_j(species) is the entropy of mixing of all species at the location of bin j, $p_{c/j}$ is the probability of finding a particle of species c conditional on the bin j, $S_{\text{locations}}$(species) is a spatial average of the entropy of mixing of species conditional on location in the image divided into N bins, and p_j is the probability of finding a particle irrespective of species in bin j. We estimated $p_{c/j}$ using the pixel reading x_j with $0 < x_j < 255$, with 0 corresponding to black and 255 to white. For the general case when the two species have different concentrations at the inlet (Section 0): white/black = optimum (if the white and black regions are equal then optimum = 1), perfect mixing should correspond to having in this particular pixel j the same ratio of white and black as in the whole system (Camesasca et al. 2006). This is accomplished by defining the following:

$$p_{1/j} = \frac{\frac{x_j}{255}}{\frac{x_j}{255} + \text{optimum} * (1 - \frac{x_j}{255})} \tag{3}$$

$$p_{2/j} = 1 - p_{1/j}. \tag{4}$$

The mixing entropy, Eq. (1), is maximum when $p_{1/j} = p_{2/j}$ or $x_j/255 = \text{optimum} * (1 - x_j/255)$. To find the mixing index, M, the entropy of mixing was normalized with $\ln(2)$, yielding values between 0 (perfect segregation) and 1 (perfect mixing):

$$M = S_{\text{locations}}(\text{species})/\ln(2). \tag{5}$$

The values of M were evaluated using Eqs. 1–5. The concentration profile images were converted to grayscale and input to the program. Because there were separate concentration profiles for species A and B, there were also two sets of M calculated, referred to as M_A and M_B, respectively.

3.3 Device fabrication

The physical micromixer device was fabricated using well-established photolithography and soft-lithography techniques as we reported elsewhere (Kothapalli and Honarmandi 2014). The device was designed using SolidWorks® and a silicon wafer containing a positive relief of this design was developed at California NanoSystems Institute (University of California, Santa Barbara) using SU-8 photoresist techniques. Polydimethylsiloxane (PDMS; Sylgard 184; Dow Corning) was used to prepare microfluidic mixer devices using replica molding techniques detailed earlier. The devices were cleaned, plasma-treated, and bonded to glass slides, to close the channels and complete the device fabrication. The general design rules for manufacturing such devices are: range of overall device thickness could be from 3 to 7 mm to accommodate the inlet and outlet tubing connectors; the number of ridges in each cycle could vary between 8 and 14; the inner width, length, and height of each ridge could vary between 25 and 50 μm, 150–250 μm, and 25–75 μm, respectively; possible flow channel height could range between 150 and 250 μm; the number of cycles could be between 6 and 15 to enable effective mixing; the width of main channel could be between 100 and 300 μm; and the depth of bottom layer of the main channel could range between 35 and 75 μm.

3.4 Experimental setup and imaging

A fluid delivery system was developed, so that tubing could be easily connected to the inlet ports of the devices. First, a 10-mL syringe (Henke Sass Wolf, 10 mL Norm-Ject) was fit to 1/8″ inner diameter PVC tubing (Clearflex 60), which in turn was fit to 1/16″ inner diameter tubing (Clearflex 60), the end of which was connected to a 90° elbow joint (McMaster-Carr) fitted to the inlet ports of the device. The effluent fluid at the outlet was collected using similar tubing and emptied into a petri dish. Each syringe was loaded into a syringe pump (Harvard Instruments PicoPlus or Razel A-99 FM) to pump fluid into the device. The pumps were both calibrated for operation at flow rates in the range of 5–500 μL/min prior to start of experiments.

The flow within the channels was imaged using a Nikon A1 Rsi confocal microscope to evaluate experimental

mixing quality. Solutions (10 μM) of 10 kDa FITC–dextran and 10 kDa rhodamine B–dextran fluorescent dyes were filled in syringes and pumped briefly to purge bubbles through the system. The pumps were set to the appropriate settings to produce the desired flow rate in the device using the appropriate calibration curves. The device was selected to operate at $Re = 10$, $R_{AB} = 1$, and $D_A = D_B = D10$. The device was stabilized under the microscope by taping to petri dish, and the respective tubes were connected to the device via the inlet and outlet ports. Both pumps were started simultaneously, fluid flow within the device was monitored as it approached steady state, and mixing of two streams was visualized in the x–z plane at various heights (y-stacks) using a 10 × objective lens. At each location, a stack of 40 images was taken to cover the height of the entire channel. Images were processed using NIH ImageJ (version 1.51j8) by merging each pair of images into a composite of two color channels.

4 Results and discussion

4.1 CFD simulations

For each study listed in Table 2, CFD simulations were performed at various sets of operating conditions, yielding spatial concentration data and plots. Except for Study 5, cross sections of the concentration profile in the channels were used to compute the mixing index M for each species at different locations. Each case within a study had a set of concentration profile (mol/L) plots and a plot of M versus section number in the device.

Rapid mixing was achieved with this channel design due to the shape of the herringbone ridges. Simulation results for the velocity profile in the channels (Fig. 3) indicated that the flow was warped and rotated about itself. Specifically, there were two counter-rotating vortices due to the vertex in each ridge, adding y and z velocity components to the flow. If there was no vertex (i.e., a slanted groove that covered the entire width of the channel), there would be one vortex about the geometric center of the channel as seen with the SGM. Figure 3 shows the velocity plots at the arbitrarily selected seventh ridge in the channel (second ridge of Section 2). These images were representative of all ridges at all locations in the studied geometry; the ridges that are in the mirrored configuration of this ridge yield a mirrored velocity field. Similar circular flow patterns were seen in the channel cross section in a forward SHB ridge configuration with the main channel height of 150 μm (Itomlenskis et al. 2008), except that the direction of rotation was opposite to that noted here.

4.1.1 Study 1: effect of Re

In Study 1, Re was varied over five orders of magnitude to determine the effect on mixing (Fig. 4). Representative concentration profiles at $Re = 0.1$, $D_A = D_B = D1$, and $R_{AB} = 1$ are shown in Fig. 4a, b. The concentration profile showed the segregated colors at the inlet becoming progressively indistinct along the simulated length. The two species were almost indistinguishable by the time they reached Sect. 6, indicating near perfect mixing. The rotational flow was clearly seen as the two species are rotated around each other. As expected, the concentration profiles between the two species were identical and $M_A = M_B$, because $D_A = D_B$. The results showed a very weak correlation between M and Re. Mixing efficiency was higher at $Re = 0.01$, possibly due to longer residence time and better diffusion.

The values of M reached 0.99 or higher by the end of Sect. 5. However, in the case of $Re = 100$, M reached 0.985 suggesting relatively low mixing quality, possibly due to shorter residence time of the fluid in the simulated length with less time for diffusion to act. Thus, it is reasonable to conclude that Re has no impact on the effectiveness of mixing in this device design. To enable predictability at intermediate points, the mixing index was fit to a two-parameter exponential rise to maximum function given by $M = a(1 - e^{-bx})$, where x is the section number (and indirectly the length of the channel) and a and b are parameters of the fit (Fig. 4c). The values of a ranged from 1 to 1.046, while that of b ranged from 1.505 to 0.6074, with both the model parameters and the overall fit being significant in all the cases ($p < 0.001$). This was also the case in the forward configuration of the SHB (Stroock et al. 2002), where the flow pattern was found to be independent of Re, for $1 < Re < 100$, as well as in Stokes flow at Re < 1 when the ratio of the ridge height to channel height (α) was less than 0.3. Our results mimic this trend, although $\alpha = 1$ for our design.

Study 2 was performed using a geometry that contained six mixing cycles to observe how mixing evolves beyond the third cycle, and the results could be seen in Fig. SI–2. This simulation was performed at $Re = 1$ with equal diffusivities in species A and B. Similar mixing trends seen in cycles 1, 2, and 3 in Study 1 were noted here. Considering that $M \geqslant 0.99$ by the time the fluid enters the fourth cycle, further changes were extremely small in the asymptotic approach to 1. Since fluid deformations in laminar flow could be undone by reversing the deformation sequence, these results indicate that the mixing continued to completion without reverting to a segregated state. The mixing within these channels is so complex that the fluid does not return to a more orderly state.
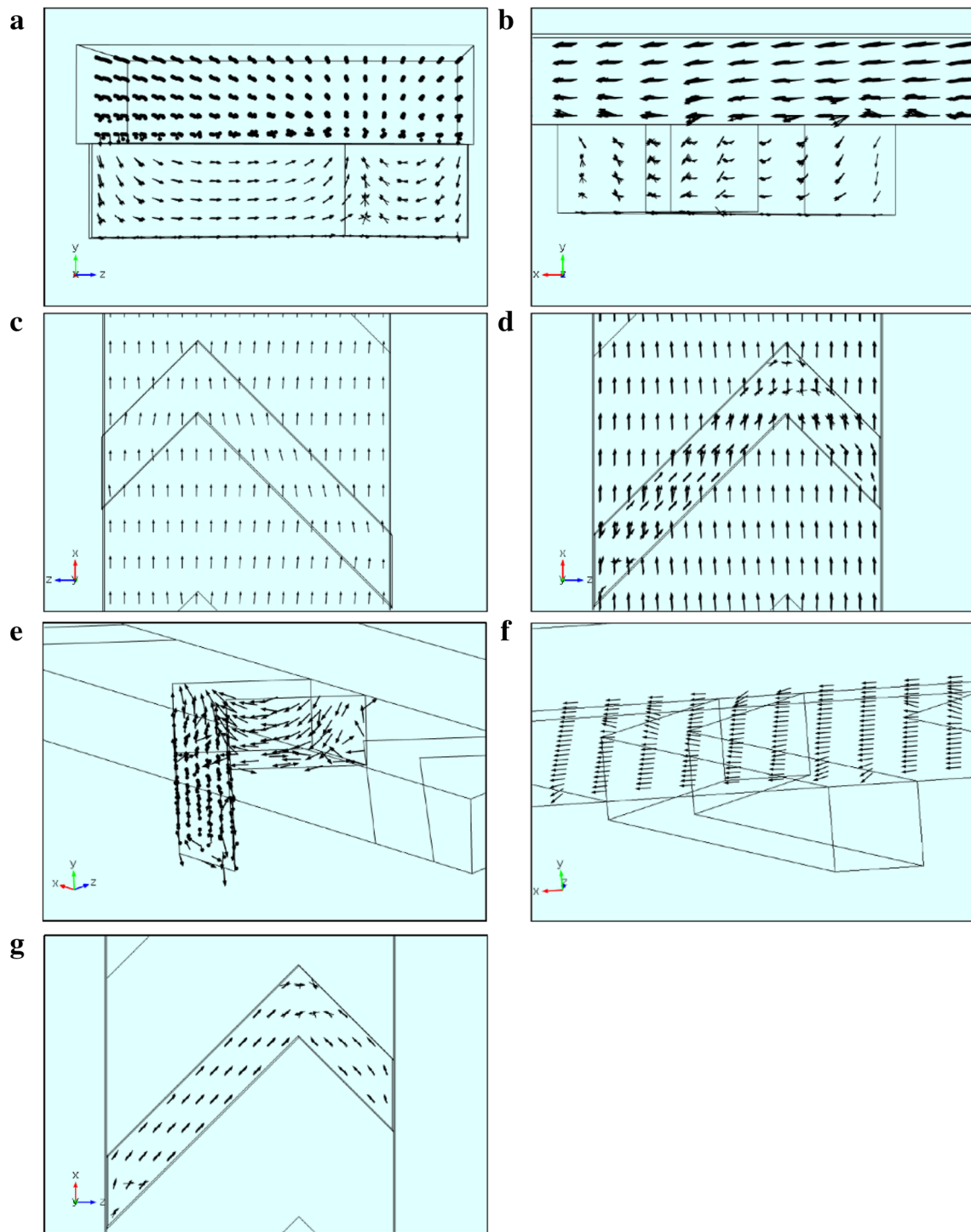
Fig. 3 **a** Velocity profile as seen in the cross section of the channel (*y*–*z* plane) shows fluid circulation from the outside walls towards the vertex of the ridge. **b** Side view (*x*–*y* plane) of the ridge shows fluid dropping downward into the ridge. The fluid moves along the ridge until it is forced upward at the vertex. **c** Top–down view (*x*–*z* plane) of the channel shows horizontal motion being imparted on the fluid as it passes over the ridge. These arrows were plotted very close to the bottom of the main channel ($y = 5$ μm). **d** This is the same view as in (c), except that the arrows were plotted at many values of *y* as in (a, b). **e** Velocity field in the ridge shows fluid entering the ridge from the outside and traveling to the vertex in a curved path. **f** Downward and upward velocity components due to the ridge can be seen more clearly by showing arrows only at $y = 5$ μm. **g** Path of the fluid moving along the ridge is evident when only the velocity field in the ridge is shown

Fig. 4 a, b Representative concentration profile in the channels at $Re = 0.1$, $D_A = D_B = D1$, and $R_{AB} = 1$. The rotational flow generated by the ridges is most evident in the first section; species A is migrating leftward toward the vertex of the ridge and species B is being forced down and to the right. **c** Mixing index data of species A for all simulated cases in Study 1. The data were fit to a two-parameter exponential rise to maximum function, and the model fit the data well ($R^2 > 0.95$) with the fit parameters being significant ($p < 0.001$) in all the cases. Identical mixing index data were obtained for species B for all cases in Study 1 (data not shown)
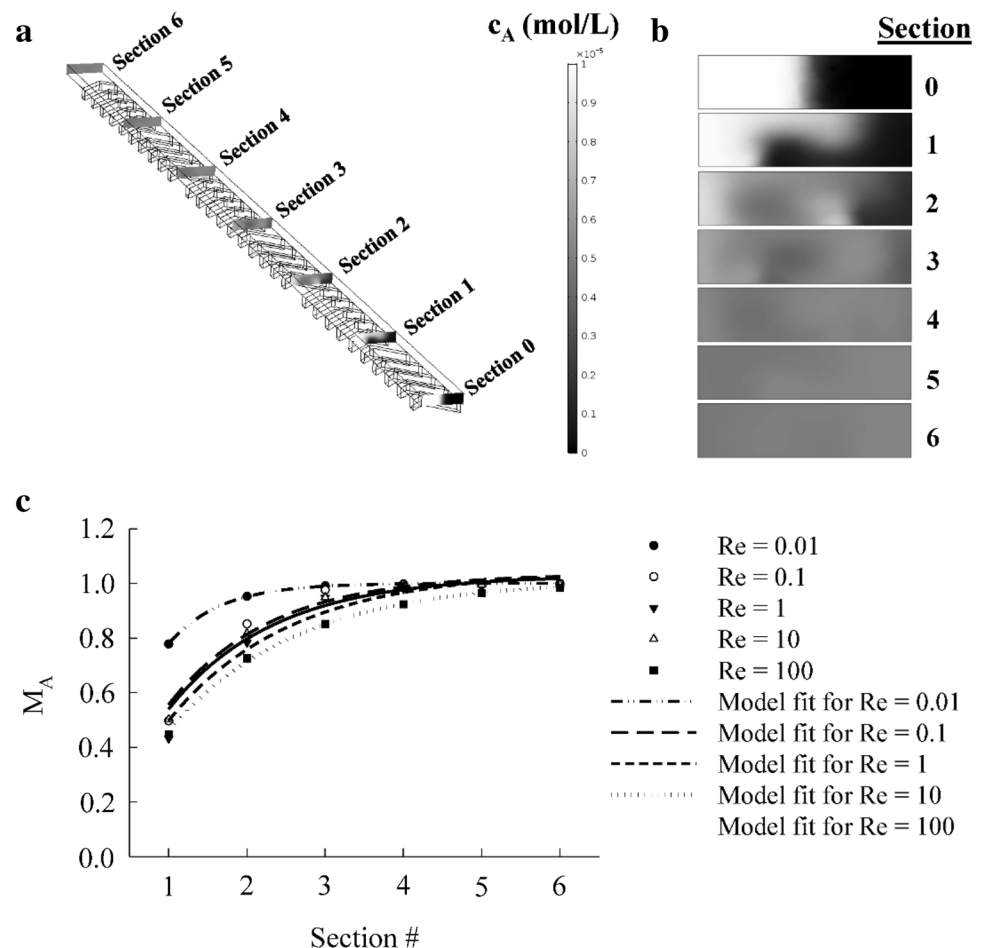
4.1.2 Study 3: effect of diffusivity

The effect of diffusivity and various combinations of species diffusivities on M was evaluated in Study 3 and representative data for a select case ($Re = 1$, $D_A = D1$, $D_B = D1000$, $R_{AB} = 1$) is shown in Fig. 5a. Such concentration profiles and mixing indices for other diffusivity pairings at other Re were computed in a similar fashion. It is apparent that the diffusion coefficient has a weak effect on the mixing efficiency; all cases investigated yielded $M \approx 0.98$ or higher by the time the fluid reached Sect. 6 (nearly identical to the results of Study 1) with the same asymptotic trend. At $D_A = D1$, M_A reached 0.989 by Sect. 4; at $D_A = D10$, M_A reached 0.98 by Sect. 5; at $D_A = D100$, M_A was at 0.989 by Sect. 5; but at $D_A = D1000$, $M_A \approx 0.989$ by Sect. 6. As mentioned previously, this is most likely due to the short residence time of fluid in the studied channel length as well as the fact that diffusion is naturally a slow process.
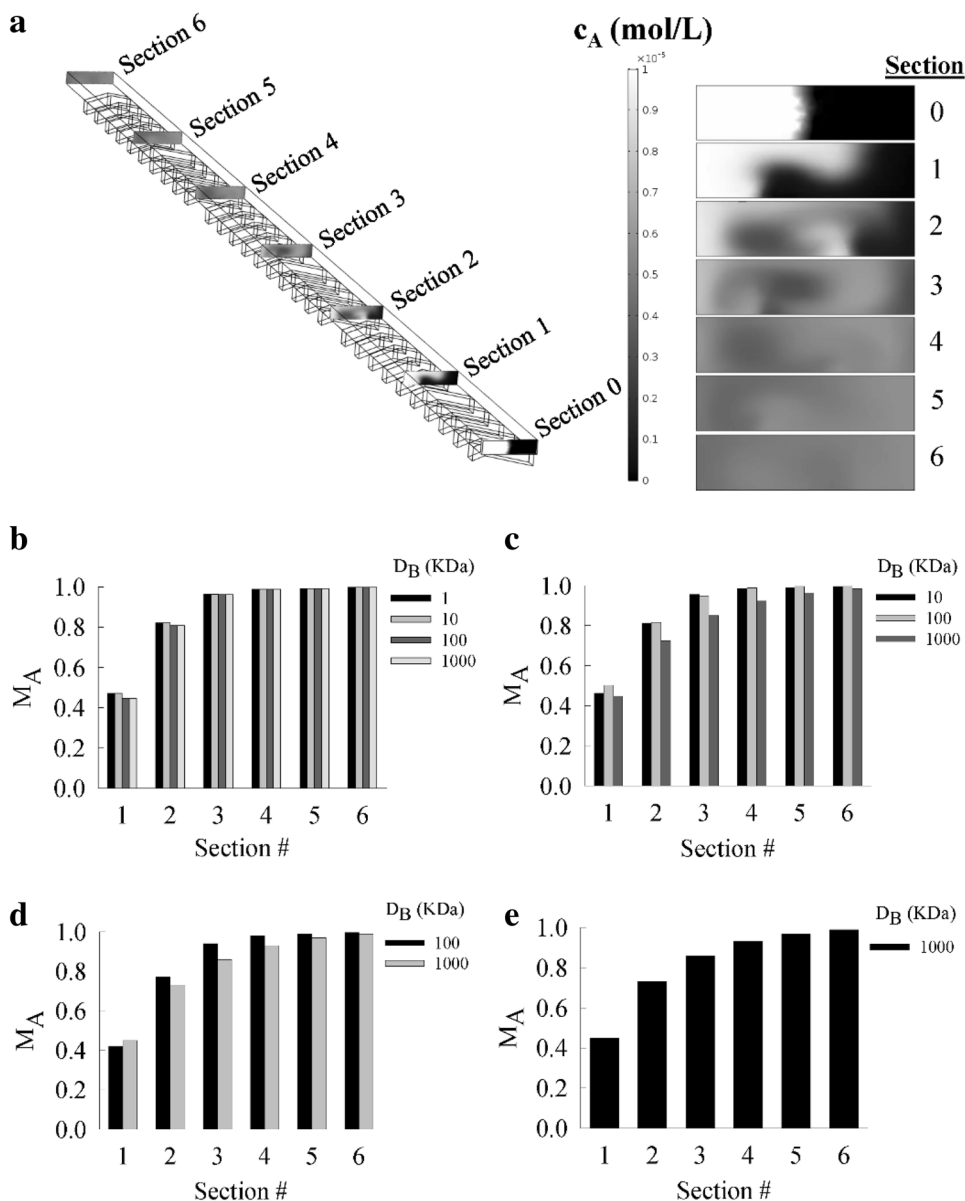
To enable predictability, M values were fit to a two-parameter exponential rise to maximum function discussed earlier. For data shown in Fig. 5b–e, the values of a ranged from 1.013 to 1.045, while that of b ranged from 0.7145 to 0.6064, with both the model parameters and the overall fit being highly significant in all the cases ($p < 0.001$). The mixing of species of considerably different diffusivities, such as in pair 4 which utilizes $D1$ and $D1000$ (Fig. 5e), does cause M to approach a value of one at a slightly lower rate than the other cases. As molecular weight increases, diffusivity decreases, so the transport of material is hindered. Our results are in broad agreement with reports by other groups. Liu et al. observed that diffusive mixing of species was enhanced at lower Re and higher diffusivity in a standard SHB (Liu et al. 2004). However, independent of the diffusivities, the overall result is largely the same in each case. Itomlenskis et al. determined that diffusion's contribution to mixing at $Re \approx 1$ is not more than 10% for the SHB mixer (Itomlenskis et al. 2008).

Our results are also in agreement with the Péclet number range in this system. The value of D was taken to be $D1$, since it was the largest. For Re at 0.01, 0.1, 1, 10, and 100; the values of Pe were 34.4, 344, 3440, 34,400, and 344,000, respectively. Clearly, $Pe \gg 1$ for all cases implying that convective transport is vastly more significant than diffusive transport, even at lower molecular weight of the diffusing species. This is within expectations, because mixing is driven by transverse flows generated by the

herringbone ridges rather than convective turbulence. The calculated Pe are also consistent with diffusion being too slow of a process to be significant in the evolution of mixing. Strook et al. (2002) investigated mixing performance of their SHB mixer as a function of Pe. Over the range of $2 \times 10^3 < Pe < 9 \times 10^5$, the channel length required for 90% mixing changed by a factor of 2.4. Although our mixer falls within this Pe range, the mixing length did not change appreciably across all cases discussed thus far. This discrepancy might be due to differences in the respective channel designs, or in the evaluation of mixing index. It is noteworthy that Strook et al. evaluated mixing index by the standard deviation of the intensity distribution from confocal images rather than calculating entropy.

4.1.3 Study 4: effect of R_{AB} on mixing efficiency

The effect of R_{AB} was investigated in Study 4, and representative results from a select case are shown in Fig. 6. It is apparent that M approached higher values in the initial sections as R_{AB} increased, across all Re values. The effect of R_{AB} appears to come into play only during the early phase of bringing the fluids together at the beginning of the channel. Since more fluid is of one species at higher R_{AB}, it becomes easier to distribute both species across the channels. Increasing R_{AB} to greater extremes (e.g., ≈ 10) would result in the minority fluid encountering much more of the other fluid, and quickly assimilating into the rest of the channel. This sliver of minority fluid would follow the rotational pattern

Fig. 6 **a** Representative concentration profile of each species in the channels at $Re = 10$, $D_A = D_B = D10$, $R_{AB} = 3$. Effect of R_{AB} on M with $D_A = D_B = D1$, and at $Re = 0.1$ (**b**), $Re = 1$ (**c**), $Re = 10$ (**d**), and $Re = 100$ (**e**). Similar concentration profiles for M_B were noted, and hence, data were not shown
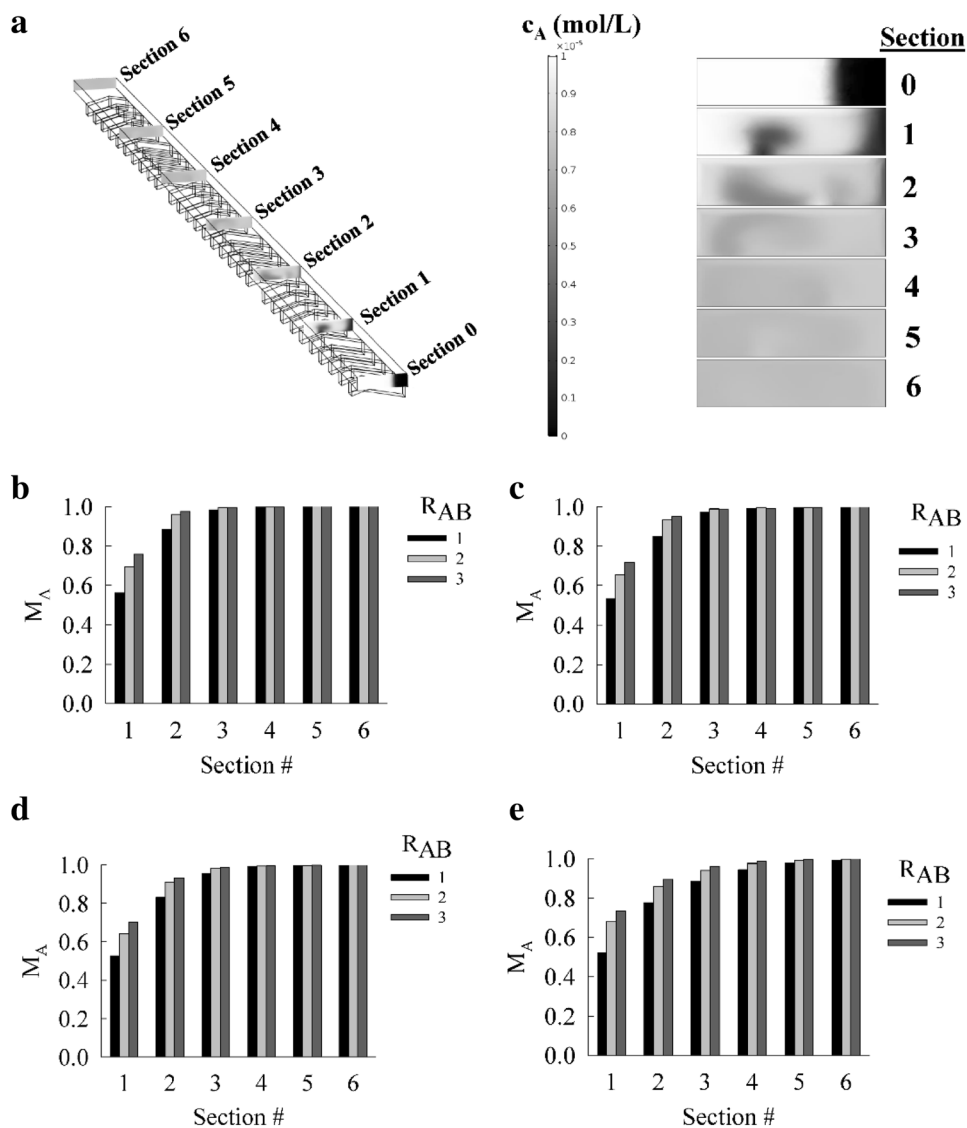

until it reaches the center where the two vortices meet and probably break up in the flow pattern at the top of the channel (some fluid goes left, some goes right), which speeds up the mixing. The values of M were fit to a two-parameter exponential rise to maximum function discussed earlier. For the data shown in Fig. 6b–e, the values of a ranged from 0.9875 to 1.0282, while that of b ranged from 0.776 to 1.45, with both the model parameters and the overall fit being highly significant in all the cases ($p < 0.001$). Interestingly, at a constant Re, the value of a decreased, while that of b increased with increasing R_{AB}.

Studies showing the effect of the flow rate ratio of the fed species seem to be very uncommon, so drawing literature comparisons was difficult. One study by Kastner et al. (2015) involved formulating liposomes from 1,2-dioleoyl-3-trimethylammoniumpropane (DOTAP) and 1,2-dioleoyl-sn-glycero-3-phosphoethanolamine (DOPE) with an SHB

mixer (200 μm-wide × 78 μm-tall channel, 50 μm-wide × 31 μm-deep ridges). The flow rate ratio (FRR) of DOTAP and DOPE was varied from 1 to 5 and the total flow rate (TFR) was varied from 0.5 to 2 mL/min. Results showed that as FRR increased, liposome size decreased, polydispersity decreased, and transfection efficacy decreased. The lower amount of solvent in the mixture resulted in production of smaller liposomes, concurring with our results that the minority fluid was spread more thinly across the channels.

4.1.4 Study 5: transient study

For the time-dependent studies, the concentration profile was observed to develop in the same manner for all Re investigated here (Fig. 7). The front of fluid, containing the species side-by-side, passed through the channel leaving behind the steady-state concentration profile seen earlier. The flow

a

b

c
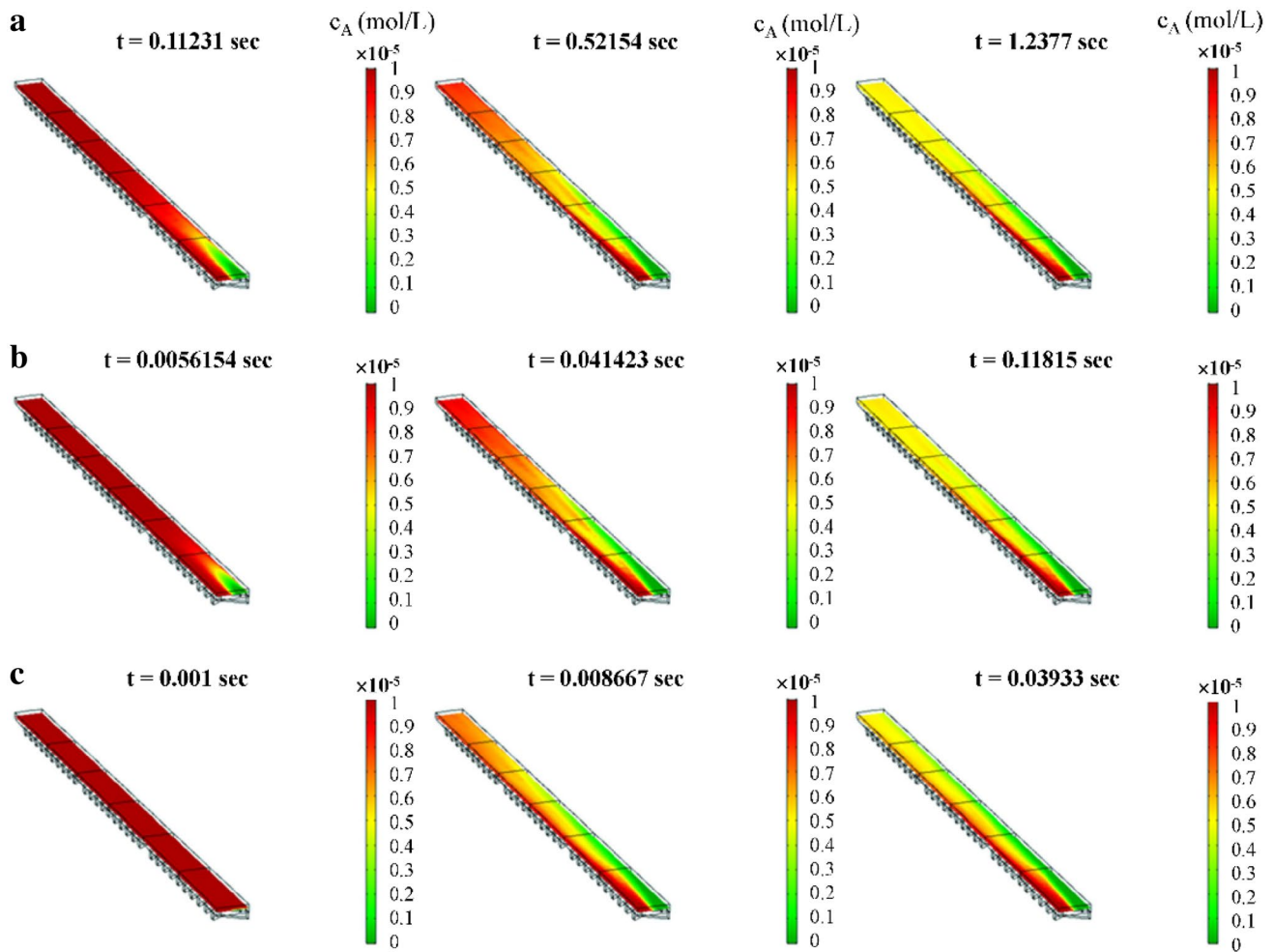
Fig. 7 Transient development of flow in the channels. **a** Time evolution of mixing for $Re = 1$, $R_{AB} = 1$, $D_A = D_B = D10$. Snapshots were taken at $t = 0.112$ s, $t = 0.521$ s, and $t = 1.24$ s. **b** Time evolution of mixing for $Re = 10$, $R_{AB} = 1$, $D_A = D_B = D10$. Snapshots were taken at $t = 0.006$ s, $t = 0.041$ s, and $t = 0.118$ s. **c** Time evolution of mixing for $Re = 100$, $R_{AB} = 1$, $D_A = D_B = D10$. Snapshots were taken at $t = 0.001$ s, $t = 0.009$ s, and $t = 0.039$ s. The first three cycles along the device length were shown in each case

pattern was not only effective at mixing but was also consistent and developed similarly each time, instantaneously. Therefore, the flow is not truly chaotic, as routinely termed in the literature for such channel designs (e.g., SHB). The only effect that Re had on the approach to the steady state was the amount of time required, i.e., the time which it took for the fluid front to pass through the outlet of the third cycle. It took 10.8, 1.24, 0.118, and 0.0393s to approach the steady state in these devices, at $Re = 0.1$, 1, 10, and 100, respectively, indicating that the time it takes to reach steady state decreased by an order of magnitude with increasing Re by an order of magnitude.

4.2 Tracing fluid flow using confocal microscopy

Confocal microscopy imaging enabled visualization of flow within the SHB channel in multiple layers, each 2-μm-thick,

along the x–z planes, allowing a direct comparison of the imaging results to CFD simulations at respective locations in each plane. For select positions along the y-axis (every 10-μm-thick), representative confocal microscopy images at Sect. 1 are shown in Fig. 8, alongside the CFD concentration profiles obtained at that location. Similar comparison of results from confocal images and CFD simulations at Sect. 2 to 6 are shown in Figs. SI-3 to SI-7. The 3D volume stack renderings of the image stacks (using ImageJ) at each section are shown in Fig. 9. Comparing the images qualitatively and quantitatively (intensity profiles, Fig. 8b, c), significant resemblances were noted between the experimental and simulated flow conditions. Similar profiles could be obtained for species B (green channel), as well as at other sections in the channels. Nearly, every detail in the concentration profile computed in COMSOL was validated in the experimental results, which makes for a strong case that the simulations accurately predicted the real behavior
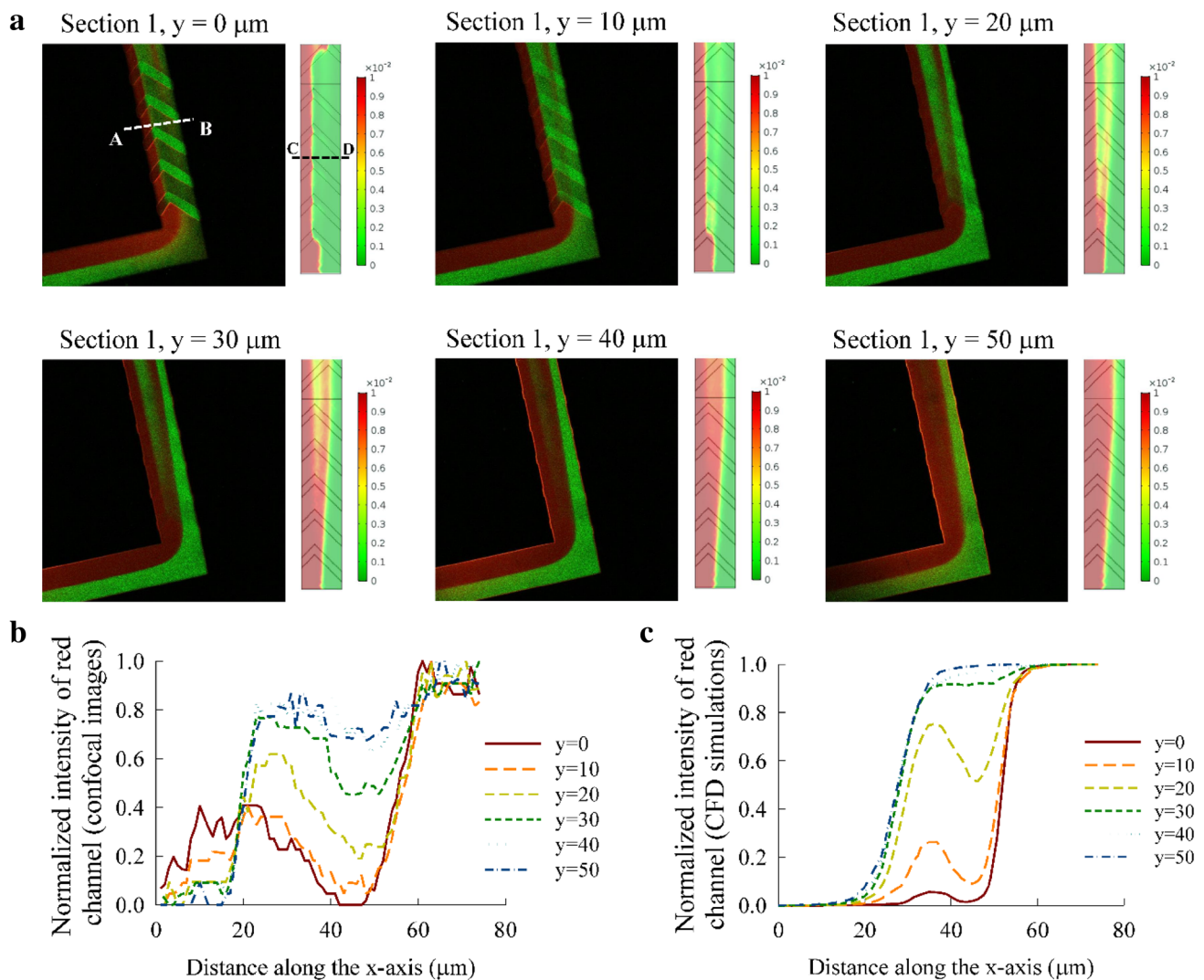
Fig. 8 **a** Representative confocal microscopy images of the fluid mixing within the device (left panels) were compared to results obtained from COMSOL based CFD simulations (right panels) at similar conditions and locations (selected). Data shown here were for Sect. 1 at $Re = 10$, $R_{AB} = 1$, and $D_A = D_B = D10$. The height position $y = 0$ corresponds to the top of the ridges. The intensity of species A (red staining) in the channels at various locations was quantified using custom-written MATLAB code from the confocal images (**b**) and CFD simulations (**c**). For the quantitative data shown here, the intensity profile at horizontal line A–B between ridges 3 and 4 in Sect. 1 of the confocal images was considered. Similarly, the intensity profile at line C-D at a similar location was taken for the images obtained from CFD simulations, to compare the outcomes between experimental (confocal imaging) and CFD simulations

of fluid flow. Among others, Amini et al. (2013) and Williams et al. (2008) have also shown that CFD simulations can accurately predict and compliment confocal microscope images, for investigating fluid flow within microfluidic channels. However, confocal microscopy images of channel cross sections in *y–z* planes would be required to calculate *M*.

5 Conclusions

A microfluidic reverse-staggered herringbone mixer was designed, fabricated, characterized, and implemented using both CFD simulations and complimentary

Fig. 9 Volumized 3D renderings of confocal image stacks at Sect. 1 to 6, obtained by merging the x–z image stacks obtained at all locations along the y-axis within that section
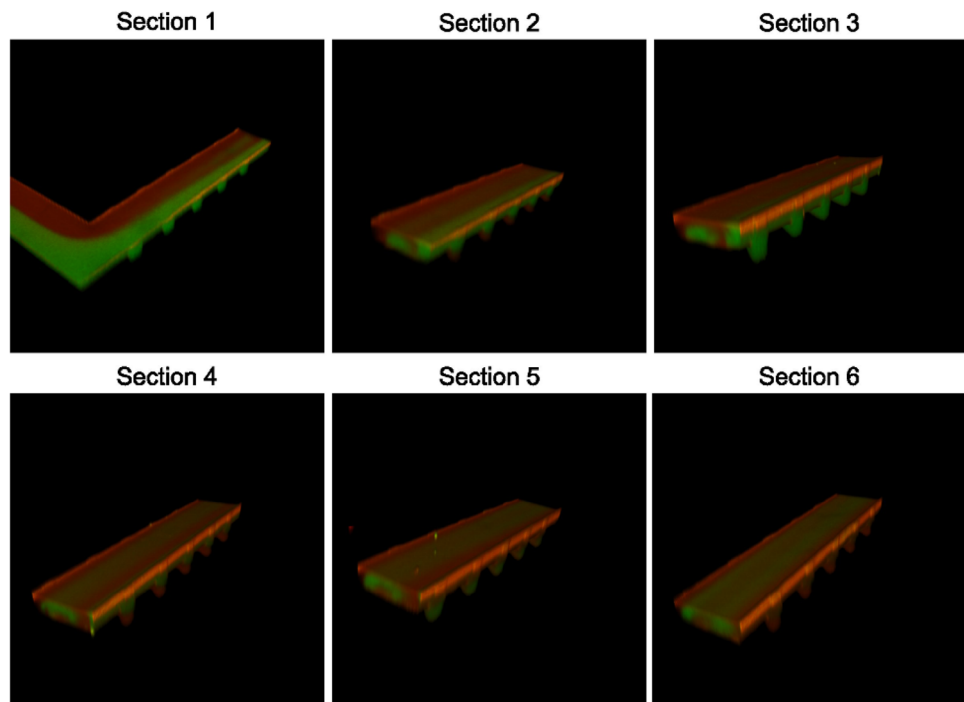
experiments, to investigate the role of various operating variables on the mixing of two fluids. Simulations predicted that mixing in the device would be nearly complete ($M \cong 1$) by the end of third mixing cycle, under most operating conditions. Among the variables tested, R_{AB} had the strongest effect on the mixing completeness within the first three cycles, Re had a very weak effect on the mixer's efficiency, while the values of D_A and D_B were virtually inconsequential to the results. Simulations in extended channel length (six cycles) indicated that mixing rapidly continued to completion, without any reversal of mixing progress. Time-dependent CFD simulations showed that steady-state flow was established quickly after fluid entered the SHB channel, and the time to reach steady-state decreased with increasing Re. The device was physically constructed using standard soft-lithography techniques and implemented in selective cases to verify the simulation predictions. CFD simulations in COMSOL accurately predicted the real behavior of fluid flow in the device, as evident from strikingly close resemblance to the confocal microscopy images at respective locations. This SHB channel design proved to be effective at thoroughly mixing two separate fluids despite the limitations imposed by laminar flow.

References

Amini H, Sollier E, Masaeli M, Xie Y, Ganapathysubramanian B, Stone HA, Di Carlo D (2013) Engineering fluid flow using sequenced microstructures. Nat Commun 4:1–8

Bellassai N, Spoto G (2016) Biosensors for liquid biopsy: circulating nucleic acids to diagnose and treat cancer. Anal Bioanal Chem 408:7255–7264

Bird RB, Stewart WE, Lightfoot EN (2006) Transport phenomena. vol Book, Whole. John Wiley & Sons, Inc., Hoboken

Camesasca M, Manas-Zloczower I, Kaufman M (2005) Entropic characterization of mixing in microchannels. J Micromech Microeng 15:2038–2045

Camesasca M, Kaufman M, Manas-Zloczower I (2006) Quantifying fluid mixing with the Shannon entropy. Macromol Theory Simul 15:595–607

Capretto L, Cheng W, Hill M, Zhang X (2011) Micromixing within microfluidic devices. Top Curr chem 304:27–68

Du Y, Zhang Z, Yim C, Lin M, Cao X (2010) A simplified design of the staggered herringbone micromixer for practical applications. Biomicrofluidics 4:024105. https://doi.org/10.1063/1.3427240

Ehrfeld W, Hessel V, Lowe H (2000) Microreactors: new technology for modern chemistry. Wiley-VCH, Weinheim

Erbacher C, Bessoth F, Busch M, Verpoorte E, Manz A (1999) Towards integrated continuous-flow chemical reactors Mikrochim Acta 131:19–24

Fodor PS, Kaufman M (2011) Time evolution of mixing in the staggered herringbone microchannel. Mod Phys Lett B 25:1111

Fodor P, Itomlenskis M, Kaufman M (2009) Assessment of mixing in passive microchannels with fractal surface patterning. Eur Phys J Appl Phys 47:31301

Giuffrida MC, Spoto G (2017) Integration of isothermal amplification methods in microfluidic devices: recent advances. Biosens Bioelectron 90:174–186

Glasgow I, Aubry N (2003) Enhancement of microfluidic mixing using time pulsing Lab Chip 3:114–120

Günther A, Jensen KF (2006) Multiphase microfluidics: from flow characteristics to chemical and materials synthesis. Lab Chip 6:1487–1503

Hessel V, Kralisch D, Krtschil U (2008) Sustainability through green processing—novel process windows intensify micro and milli process technologies. Energy Environ Sci 1:467–478

Itomlenskis M, Fodor PS, Kaufman M (2008) Design of Passive Micromixers using the COMSOL Multiphysics software package. In: Proceedings of the COMSOL Conference 2008 Boston

Janasek D, Franzke J, Manz A (2006) Scaling and the design of miniaturized chemical-analysis systems. Nature 442:374–380

Jeong GS, Chung S, Kim CB, Lee SH (2009) Applications of micromixing technology. Analyst 135:460–473

Johnson T, Ross D, Locasio LE (2002) Rapid microfluidic mixing. Anal Chem 74:45–51

Kamholz AE, Weigl BH, Finlayson BA, Yager P (1999) Quantitative analysis of molecular interaction in a microfluidic channel: the T-sensor. Anal Chem 71:5340–5347

Kamholz AE, Schilling EA, Yager P (2001) Optical measurement of transverse molecular diffusion in a microchannel. Biophys J 80:1967–1972

Kastner E, Kaur R, Lowry D, Moghaddam B, Wilkinson A, Perrie Y (2015) High-throughput manufacturing of size-tuned liposomes by a new microfluidics method using enhanced statistical tools for characterization. Int J Pharm 477:361–368

Kaufman M, Camesasca M, Manas-Zloczower I, Dudik LA, Liu C (2007) Applications of statistical physics to mixing in microchannels: entropy and multifractals. In: Vaseashta A, Mihailescu I (eds) Proceedings of NATO Advanced Study Institute: Functionalized Nnanoscale Materials, Devices and Systems for Chem-Bio Sensors, Photonics, and Energy Generation and Storage, 2007. Springer NATO Science for Peace and Security Series Physics and Biophysics, pp 437–444

Kee SP, Gavriilidis A (2008) Design and characterisation of the staggered herringbone mixer. Chem Eng J 142:109–121

Knight J, Vishwanath A, Brody J, Austin R (1998) Hydrodynamic focusing on a silicon chip: mixing nanoliters in microsecond. Phys Rev Lett 80:3863–3866

Kothapalli CR, Honarmandi P (2014) Theoretical and experimental quantification of the role of diffusive chemogradients on neuritogenesis within three-dimensional collagen scaffolds. Acta Biomater 10:3664–3674

Kwak TJ, Nam YG, Najera MA, Lee SW, Strickler JR, Chang W (2016) Convex grooves in staggered herringbone mixer improve mixing efficiency of laminar flow in. Microchannel Plos One 11:1–15

Lee S, Kim D, Lee S, Kwon T (2006) A split and recombination micromixer fabricated in a PDMS three-dimensional structure. J Micromech Microeng 16:1067–1072

Li P, Cogswell J, Faghri M (2012) Design and test of a passive planar labyrinth micromixer for rapid fluid mixing. Sens Actuators B 174:126–132

Liu YZ, Kim BJ, Sung HJ (2004) Two-fluid mixing in a microchannel. Int J Heat Fluid Flow 25:986–995

Makgwane PR, Ray SS (2014) Synthesis of nanomaterials by continuous-flow microfluidics: a review. J Nanosci Nanotechnol 14:1338–1363

McCabe WL, Smith JC, Harriot P (2004) Unit operations of chemical engineering. vol Book, Whole. McGraw-Hill Education, Philadelphia

Nguyen NT, Wu Z (2005) Micromixers—a review. J Micromech Microeng 15:R1–R16

Nimafar M, Viktorov V, Martinelli M (2012) Experimental investigation of split and recombination micromixer in confront with basic T- and O- type. Micromixers Int J Mech Appl 2:61–69

Özbey A, Karimzadehkhouei M, Akgönül S, Gozuacik D, Koşar A (2016) Inertial focusing of microparticles in curvilinear microchannels. Sci Rep 6:1–11

Salmanzadeh A, Shafiee H, Davalos RV, Stremler MA (2011) Microfluidic mixing using contactless dielectrophoresis. Electrophoresis 32:2569–2578

Spoto G, Corradini R (2012) Detection of non-amplified genomic DNA. vol Book, Whole. Springer Science & Business Media, Berlin

Stremler MA, Haselton FR, Aref H (2004) Designing for chaos: applications of chaotic advection at the microscale. Phil Trans R Soc Lond A 362:1019–1036

Stroock AD, Dertinger SKW, Ajdari A, Mezic I, Stone HA, Whitesides GM (2002) Chaotic mixer for microchannels. Sci Mag 295:647–651

Sudarsan AP, Ugaz VM (2006) Multivortex micromixing. Proc Natl Acad Sci 103:7228–7233

Tan WH, Suzuki Y, Kasagi N, Shikazono N, Furukawa K, Ushida T (2005) A lamination micro mixer for micro-immunomagnetic cell sorter. JSME Int J Ser C 48:425–435

Toonder JD et al (2008) Artificial cilia for active micro-fluidic mixing. Lab Chip 8:533–541

Tsai J, Lin L (2001) Active microfluidic mixer and gas bubble filter driven by thermal bubble micropump. Sens Actuators A 97:665–671

Welty JR, Wicks CE, Wilson RE, Rorrer GL (2008) Fundamentals of momentum, heat, and mass transfer. vol Book, Whole. John Wiley & Sons, Inc., Hoboken

Williams MS, Longmuir KJ, Yager P (2008) A practical guide to the staggered herringbone mixer. Lab Chip 8:1121–1129. https://doi.org/10.1039/b802562b

Wu Z, Nguyen NT (2005) Convective–diffusive transport in parallel lamination micromixers. Microfluid Nanofluid 1:208–217

Xia HM, Wan SYM, Shu C, Chew YT (2005) Chaotic micromixers using two-layer crossing channels to exhibit fast mixing at low Reynolds numbers. Lab Chip 5:748–755

Yang Z, Matsumoto S, Goto H, Matsumoto M, Maeda R (2001) Ultrasonic micromixer for microfluidic systems. Sens Actuators A 93:266–272

Yaralioglu G, Wygant I, Marentis T, Khuri-Yakub B (2004) Ultrasonic mixing in microfluidic channels using integrated transducers. Anal Chem 76:3694–3698